Arabian Journal of Chemistry (2023) **16**, 104752

King Saud University

Arabian Journal of Chemistry

www.ksu.edu.sa
www.sciencedirect.com

ORIGINAL ARTICLE

(1 1 1)-Oriented crystalline plane MnO loaded by biomass carbon separator to facilitate sulfur redox kinetics in lithium–sulfur batteries

Xusheng Gong [a,1], Rong Li [b,1], Hongguo Chen [a,2,*], Chao He [c,2,*], Zi'ang Gao [d], Haijiao Xie [e]

[a] *School of Nuclear Technology and Chemistry & Biology, Hubei Key Laboratory of Radiation Chemistry and Functional Materials, Hubei Engineering Research Center for Fragrant Plants, Hubei University of Science and Technology, Xianning, Hubei 437100, China*
[b] *Low-Carbon Technology and Chemical Reaction Engineering Laboratory, School of Chemical Engineering, Sichuan University, Chengdu 610065, China*
[c] *Hubei Key Laboratory of Petroleum Geochemistry and Environment, College of Resources and Environment, Yangtze University, Wuhan 430100, China*
[d] *Department of Naval Architecture, Ocean and Structural Engineering, School of Naval Architecture, Ocean and Energy Power Engineering, Wuhan University of Technology, Wuhan 430063, China*
[e] *Hangzhou Yanqu Information Technology Co., Ltd, Y2, 2nd Floor, Building 2, Xixi Legu Creative Pioneering Park, No. 712 Wen'er West Road, Xihu District, Hangzhou City, Zhejiang Province 310003, China*

Received 7 July 2022; accepted 24 February 2023
Available online 2 March 2023

KEYWORDS

Lithium-sulfur batteries;
Crystal planes;
Anchoring;
Catalytic ability;
Kinetic reaction

Abstract Lithium-sulfur batteries have gained widespread attention due to their high theoretical energy density. However, the insulating properties of the charge–discharge products and slow kinetic transformation result in poor rate performance of these batteries. To address this issue, a study utilized Density-functional theory calculations to predict the formation of MnO on biochar derived from Phragmites australis. Additionally, the study investigated the adsorption energy and catalytic ability of MnO with different crystal planes for lithium polysulfide. Notably, the MnO (1 1 1) crystal plane exhibited the highest chemical adsorption energy. The study also analyzed the anchoring and catalytic method of lithium polysulfides. Furthermore, advanced analytical

* Corresponding authors.
E-mail addresses: gxs5339@stu.hubu.edu.cn (X. Gong), 337691843@qq.com (R. Li), Chen_Hongguo1969@163.com (H. Chen), hechao@yangtzeu.edu.cn (C. He), gaoziang_wut@163.com (Z. Gao), xiehaijiao@shiyanjia.com (H. Xie).
[1] These authors contributed to the work equally and should be regarded as co-first authors.
[2] These authors contributed to the work equally and should be regarded as corresponding authors.

Peer review under responsibility of King Saud University.

Production and hosting by Elsevier

https://doi.org/10.1016/j.arabjc.2023.104752

methods were employed to examine the structure and morphology of biomass carbon loaded with MnO, and a separator made from MnO-loaded biomass carbon was developed for use in Li-S batteries. The findings indicate that the separator substantially enhances the kinetic reaction, resulting in exceptional rate performance.

1. Introduction

Lithium-sulfur batteries have attracted attention because of their high theoretical energy density. Different from the intercalation/deintercalation mechanism of conventional power batteries, the charge–discharge process of lithium-sulfur batteries applies the electrochemical reaction between elemental sulfur and metallic lithium to generate chemical energy and electrical energy (Zhang et al., 2023; Yucheng et al., 2023; Xiaowan et al., 2023; Xiaohui et al., 2023; Wei et al., 2023). Concerning converted chemical power sources, the traditional reaction includes the conversion of two different states of sulfur components, namely, liquid–liquid conversion and liquid–solid conversion. Lithium polysulfide tends to generate "shuttle effect" during the liquid–liquid conversion stage, causing the loss of battery active species (Yang et al., 2018; Mohan et al., 2016; Li et al., 2020; He et al., 2023; Li et al., 2021). Meanwhile, the insulating properties of the charge–discharge products and the slow kinetic transformation led to the poor rate performance of Li-S batteries. In this case, lithium-sulfur batteries can only be charged and discharged at extremely low currents under commercial conditions, seriously hindering the further commercial application of lithium-sulfur batteries (Louli et al., 2021; Zheng et al., 2018; Zhao et al., 2018; Zhang et al., 2018; He et al., 2022). In previous studies, some cathode sulfur carriers were employed to enhance the kinetics of Li-S batteries, and a micro-nanoreactor with $Ni_2Co_4P_3$ nanowires as the catalyst was designed to maximize the effectiveness of the catalyst. The composite structure rooted the $Ni_2Co_4P_3$ nanowires on the metal conductive framework, which is conducive to unfolding the metal structure, and maximizing electron conduction and charge transfer. The nanowires possess high catalytic activity, which improves the polysulfide to a great extent. For the transformation reaction of the compound (Shen et al., 2020), Dan Luo developed a novel zinc-based MOF porous nanosphere as a dynamic catalyst for lithium-sulfur batteries to accelerate the reaction kinetics of sulfur reduction. This material not only inherits the characteristics of large specific surface area and rich pore structure of MOF materials, but also exposes abundant metal nodes as active sites due to the lack of ligands to improve the adsorption and conversion of lithium polysulfides (Luo et al., 2022). In general, these methods have significantly enhanced the kinetics of lithium-sulfur batteries. Xinyu Shi and his colleagues prepared a three-dimensional (3D) multifunctional C@SnS_2 compound material separator. Using chemical etching technology, vacancies and activated carbon sites favorable for the uniform growth of SnS_2 were constructed from ZIF-67 in one step. Due to its unique structure, this C@SnS_2 structure combines electrochemical kinetics and anchored catalytic transformation of polysulfides, exhibits a synergistic effect between the porous carbon matrix and polar SnS_2 as well as achieves excellent electrochemical performance (Shi et al., 2021).

As we all know, Mn is a common transition metal element, which is extensively in various fields due to its abundant reserves, low cost, and natural catalytic activity (Cao et al., 2017). In some previous reports, it was considered that in comparison with most carbon materials, the positions of Mn and O active sites in transition metal Mn oxides are in good consistence with the positions of Li and S atoms in polysulfides (Liang et al., 2015). Therefore, it exhibits better catalytic and chemisorption properties, which can better anchor LiPSs and accelerate their redox kinetics. At the same time, *Phragmites australis* is a common aquatic emergent plant, which grows rapidly and forms a belt with its super reproductive ability and covers the shoreline. During the autumn, the material of the dead *Phragmites australis* biomass cannot be used effectively, leading to resource waste and environmental pressure. Biomass carbon made by *Phragmites australis* is a low-cost and easy-to-obtain large-scale renewable carbon source, which can be taken as a carrier to support the catalytic host (Manasa et al., 2020), and can lower Mn_2O_3 to MnO with higher catalytic capacity. Based on the above considerations, density-functional theory (DFT) calculations were performed to predict the structure of MnO on biomass charcoal, the adsorption and catalytic ability of different MnO crystal faces to Li-PSs as well as the interaction mode of the optimal crystal face with Li-PSs.

DFT results demonstrate that the (1 1 1) face of single-crystal MnO has a higher surface energy and can be more easily exposed on the surface of biomass carbon. At the same time, the (1 1 1) planes are featured with the strongest chemical anchoring and catalytic ability of Li-PSs relative to other planes, when the chemical anchoring of Li-PSs inhibits its migration, while the catalysis accelerates the transformation, both of which can suppress the "shuttle effect" and accelerate the kinetic reaction. DOS calculations further demonstrate that the main orbital components of surface anchored Li_2S_6 are the p orbital of the surface Mn element and that of element S of Li_2S_6. In addition, there are two mechanisms for the anchoring of lithium polysulfides to MnO (1 1 1). One was the antibonding interaction for the occupied orbitals between Li_2S_6 and the MnO, which contributed little to the net interaction. The other played the major roles that the frontier-orbital electron of Li_2S_6 transferred to the empty orbital (spin down) of Mn. The existence of these two interactions favors the decomposition of lithium polysulfides. In the meanwhile, biomass carbon possesses extremely high physical adsorption capacity. Therefore, preparing a biochar membrane (BCM) with strong adsorption capacity and excellent catalytic activity using manganese oxide and biomass as precursors provides an effective strategy of obtaining high-performance and stable Li-S batteries.

The experimental results reveal that the BCM features strong anchoring ability and good activation ability to Li-PSs, which may facilitate the capture and conversion of Li-PSs. When the BCM is used as a separator for Li-S batteries, it facilitates electron/ion transport, and traps Li-PSs to delay the "shuttle effect", which can simultaneously enhance the reaction kinetics of Li-S batteries. BCM separators provide high capacity and excellent long-term stability under high-rate cycling for lithium-sulfur batteries. Due to the low cost of raw materials and the simple process, this sulfur carrier is expected to facilitate the practical application of lithium-sulfur batteries, thereby improving the performance of energy storage devices on a large scale.

2. Results

Since lithium-sulfur batteries are a typical chemical reaction, promoting this reaction is the key to improving battery kinetics (Shi et al., 2021). The adsorption of Li_2S_6 (Fig. 1b) on the surface was crucial process of the elementary reaction of lithium-sulfur battery and Li_2S_6 is the main factor leading to shuttle effect. The adsorption models of Li_2S_6 on different MnO surfaces were optimized and the adsorption energy were calculated. Three typical surfaces of MnO including (2 0 0),

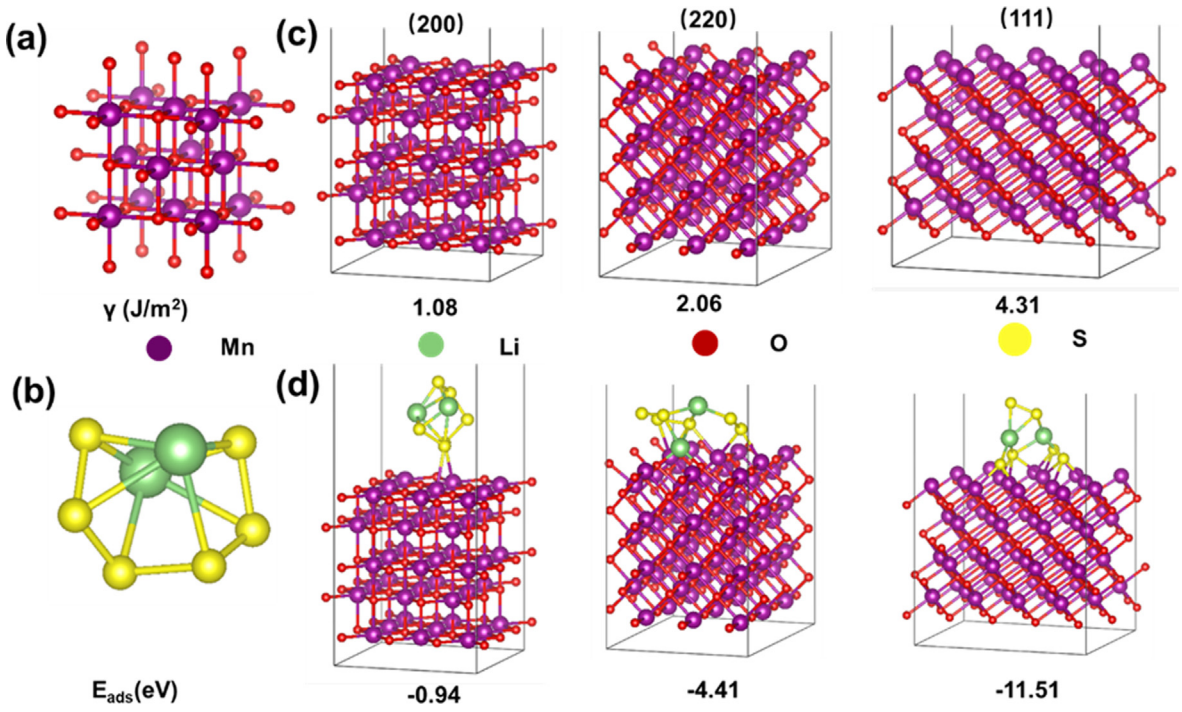

Fig. 1 a) the crystal model of MnO, b) the molecular model of Li_2S_6, c) the slab models of different facets of MnO and corresponding surface energies (γ), and d) the adsorption model of of Li_2S_6 on different crystal facets and corresponding adsorption energies (E_{ads}).

(2 2 0) and (1 1 1) were selected in calculation, corresponding to the major peaks shown in XRD patterns. As shown in Fig. 1c, the surface energies γ (J/m2) of MnO (1 0 0), (1 1 0) and (1 1 1) are 1.08, 2.06 and 4.31, accordingly, indicating that the single crystal (1 1 1) face of MnO has a higher surface energy (, 1016). Therefore, MnO in the form of single crystal MnO with the (1 1 1) plane on the surface of biomass carbon has the most unsaturated coordinating Mn sites.

The adsorption energy (Eads) of MnO (1 0 0), (1 1 0) and (1 1 1) are −0.94 eV, −4.41 eV and −11.51 eV, respectively, manifesting that MnO (1 1 1) exposed on the biomass char has the largest chemisorption energy, which can adsorb lithium polysulfides (Fig. 1d). At the same time, by comparing the lithium polysulfide bond lengths before and after adsorption (Table S1), it can be seen that before adsorption, I(Li-S) = 2.39 Å and I(S-S) = 2.0380(0) Å, while after adsorption (Fig. 2a), I(S-Li) = 2.4297(0) Å and I(S-S) = 2.0340(0) Å, which shows the bond length changes little, indicating that lithium polysulfide cannot occur on the (1 0 0) plane catalytic reaction (Li et al., 2019). After MnO(1 1 0) adsorption, I(S-Li) = 3.7788(0) Å, and I(S-S) = 2.0970(0) Å, implying that MnO(1 1 0) dominantly promotes the breaking of S-Li bonds, and it is of great importance for lithium-sulfur batteries. Here, it should be noted that the breaking of the S-S bond is the key to the transformation of long-chain lithium polysulfides into short-chain lithium polysulfides, showing that the MnO (1 1 0) crystal face is not an ideal catalytic direction for the decomposition of lithium polysulfides. Similarly, after MnO (1 1 1) adsorption (Fig. 2c), I(S-Li) = 2.6176(0) Å, and I(S-S) = 3.7735(0) Å. The S-S bond lengthening demonstrates that the conversion of long-chain lithium polysulfides to short-chain lithium polysulfides is enhanced to a great extent. In this case, combined with the above surface energy analysis, it can be concluded that MnO with (1 1 1) surface exposed on biomass carbon has an excellent selective catalytic effect on the conversion of long-chain lithium polysulfides to short-chain lithium polysulfides (Chang et al., 2018).

The strong interaction between Li_2S_6 and MnO (1 1 1) surface originated from the orbital interaction. To investigate the interaction mode, the DOS of the adsorption model of lithium polysulfide on MnO (1 1 1) before and after was calculated and analyzed (Fig. 2). Only the contribution of topmost atoms of MnO was considered to clearly represent the major change of the adsorbent. The full range of DOS results are shown in Fig. S1a. The vacuum energy level of the molecular system and the MnO surface was aligned. After adsorption of lithium polysulfide, the Fermi level increased from −1.19 eV to −0.73 eV, and the vacuum level increased from 7.92 eV to 8.46 eV, so that the work function changed slightly (9.15 to 9.19 eV). There was no need to shift the energy levels of MnO and Li_2S_6-adsorbd MnO before and after adsorption. In Fig. 2, the Fermi level of all systems moved to zero. The lithium polysulfide model after adsorption was separated in the lattice of the adsorption model and re-calculate the DOS. The comparison of the DOS of the molecular Li_2S_6 was shown in Fig. S1b. The change of the molecular orbital was attributed to the change of the geometric structure. It's observed that the energy level of the molecule after adsorption matched well with the surface models.

The spin polarization calculation resulted in the separated spin-up and spin-down electronic bands. The spin-up bands majorly located in the valence band, and the spin-down bands located in the conduction band. The spin-up and spin-down bands caused different interaction mode between adsorbed molecule and surface atoms. Spin-up orbital interactions (-6. 6 ∼ -4.1 eV) resulted from the energy band interaction between

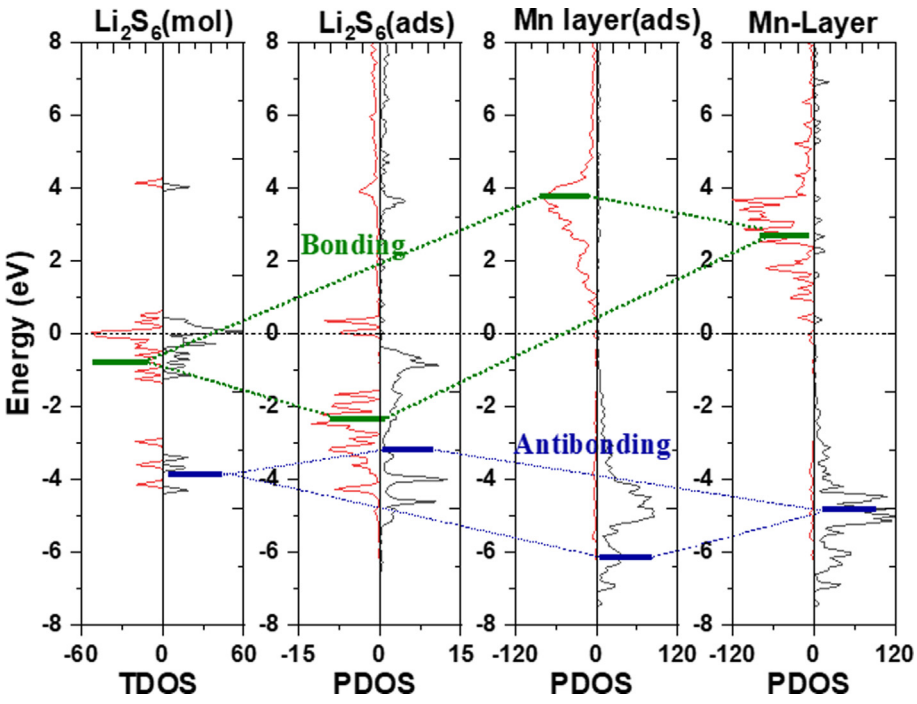

Fig. 2 TDOS and PDOS (projected density of states) diagrams of lithium polysulfide adsorbed on the MnO (1 1 1) crystal plane. From left to right, molecular TDOS before adsorption, molecular PDOS after adsorption, upmost atomic layer PDOS after adsorption, and PDOS before adsorption.

the deep-level orbitals of molecular Li_2S_6 (around −4.0 eV) and the surface states of Mn atoms on the surface (-6.7 ∼ -4. 1 eV). After the interaction, partial energy levels of Li_2S_6 (up electrons) increases, the band region of Mn atoms changed less. To specify this interaction, the DOS and COHP of the selected Mn and S atoms for one formed bond between Li_2S_6 and surface Mn atoms were analyzed (Figure S2). Weak interaction compared to that of spin-down was observed for the less negative ICOHP value (up: −0.26 eV, down: −0.53 eV), which was ascribed to the strong antibonding interaction (-3.5 ∼ -1.5 eV) under Fermi level. Therefore, the attraction between Li_2S_6 and Mn surface was from the spin-down interaction.

The spin-down interaction corresponds to a relatively higher and broader energy interval (-3.5 ∼ -1.5 eV in VB and 1.2 ∼ 5.1 eV in CB). The orbital of Li_2S_6 decreased from the interval of −1.5 ∼ 0 eV to the interval of −3 ∼ -1.5 eV after the interaction. The empty band of surface Mn increased about 1 eV. The COHP result convinced this interaction as the bonding interaction. The electron from Li_2S_6 transferred to MnO surface and filled the empty bands of surface Mn atoms (Zhang et al., 2019). In conclusion, there were two mechanisms for the anchoring of lithium polysulfides to MnO (1 1 1). One was the antibonding interaction for the occupied orbitals between Li_2S_6 and the MnO, which contributed little to the net interaction. The other played the major roles that the frontier- orbital electron of Li_2S_6 transferred to the empty orbital (spin down) of Mn. Here, it can be observed that the existence of these two interactions is conducive to the decomposition of lithium polysulfides (Wu et al., 2022).

To clarify the interaction in the orbital interactions, the PDOS and COHP analysis of Li_2S_6 and MnO after adsorption was made Figure S3-S6. Figure S3 shows that the p orbital of Li_2S_6 molecule and d band of MnO majorly contributed to the frontier orbitals. The PDOS analysis of Mn-S bond also supported this fact (Figure S4) (Zu et al., 2016). The COHP analysis in orbital resolution suggested the weak interaction between Mn and S in spin-up interaction was ascribed to the interaction of Mn 4 s and S 3p, while the interaction of Mn 3d and S 3p offset because of the low antibonding band under Fermi level. For the spin-down interaction, both of Mn 3d and Mn 4 s orbital interacted with S 3p orbital and the contribution was close (ICOHP = -0.23) (Guo et al., 2020).

The sintered biomass carbon-Mn_2O_3 was judged by XRD. As shown in Figure S7, the XRD results were perfectly matched with MnO (PDF#89–2804), when the (1 1 1), (2 0 0), (2 2 0), (3 1 1) and (2 2 2) crystal face appeared. This process can be described as the biochar acting as the reducing carbon, reducing 3-valent manganese to 2-valent manganese and dispersing it on the surface of the biomass char (Fig. 3).

Then, transmission electron microscopy (TEM) was applied to study the microstructure. The TEM images are shown in Fig. 3a, it can be clearly found that there are obvious white lumpy substances on the carbon base material. Combined with the results of eds-mapping (Fig. 3b)) and XRD results, it can be found that these white lumps are MnO. As expected, the distribution of MnO is featured with strong catalytic ability on the biomass char. Eds-mapping displays that biomass carbon contains a certain K element, and K is frequently used as a vital component of chemical activators to activate biochar. In addition, the prepared activated carbon pore structure is developed, when the specific surface area is large and the yield is high (Wu et al., 2021; Nair et al., 2020; Wang et al., 2016). At the same time, the uniform C element and bulk distribution of Mn element can be found, which is beneficial for the adsorption of lithium polysulfide by biomass carbon. This

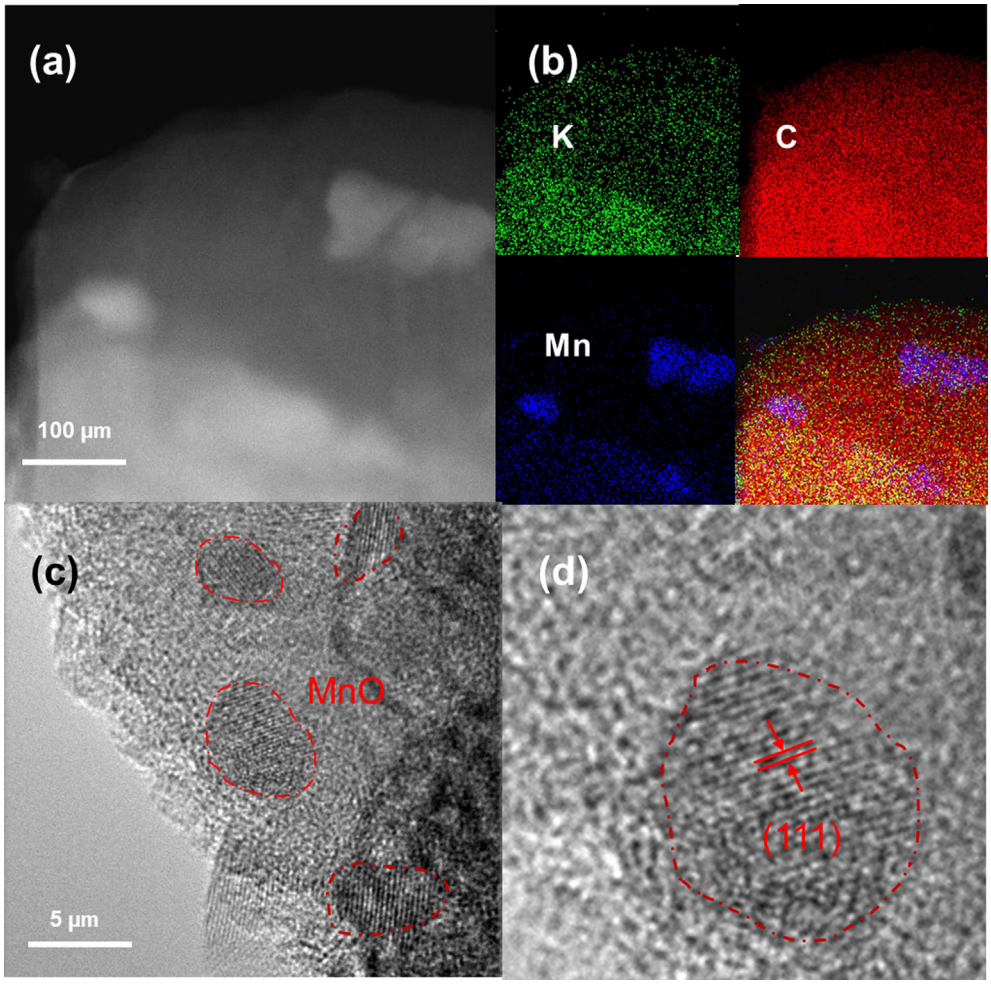

Fig. 3 a) tem image of MnO-loaded biochar, b) eds-mapping of different elements, c) schematic diagram of bulk MnO, d) schematic diagram of (1 1 1) crystal plane.

phenomenon appears in a small scale (Fig. 3c). We can see that there are no lattice stripes in most of the materials, and these areas can be judged as biomass carbon. At the same time, a small number of regions with lattice stripes appeared. Combined with the results of eds-mapping and XRD, we can infer that this is MnO. Furthermore, we measured the lattice spacing. Comparison with the standard card shows that the exposed crystal plane is the (1 1 1) crystal plane (Fig. 3d). As predicted in the DFT, the (1 1 1) plane was exposed on the biochar surface due to its higher surface energy, which can give full play to the advantages of porous biological carbon adsorption and the catalytic advantages of MnO. It can also be seen from Figure S8 that the exposed surface is mainly (1 1 1) crystal plane.

The biochar-MnO loaded separators are displayed in Fig. 4a–e. It can be seen that the biochar is distributed on the surface of the separators, and provides a natural adsorption host for the adsorption of lithium polysulfides. Based on Fig. 4d and e, we can clearly see the rod-shaped biomass. At the same time, it can be found that the particle size distribution of biomass carbon on the membrane is relatively wide. These separators with large specific surface area can uniformly disperse the lithium ions shuttled from the negative electrode side, thereby increasing the lithium ions in contact with the active material during the solid–liquid conversion and liquid–solid conversion of lithium polysulfide nucleation. This further promotes the reaction kinetics of the lithium sulfur battery. Meanwhile, EDS-mapping presented (Fig. 4f–n) that the prepared biomass carbon had a certain k due to the natural growth conditions of *Phragmites australis*. Meanwhile, it can also be observed that the distribution of the Mn element is consistent with the biomass carbon, indicating that the Mn element has been well doped into the biomass carbon. The uniform MnO distribution can better improve the kinetics of Li-S batteries.

The XPS results are shown in Fig. 5, and the full spectrum is displayed in Fig. 5a. It can be seen that there are F 1 s peaks, F 2p peaks, O 1 s peaks, C 1 s peaks, In 3 s peaks, Fe 2p and K 3 s peaks. This shows that the biomass carbon is rich in heteroatoms and makes a good effect on the adsorption of lithium polysulfide. The strong O (532.4 eV) peak originates from the biomass carbon surface layer, which indicates that Mn is dispersed on the biomass carbon surface together with the SEM results. Mn elements are divided into Mn 2p1/2 peaks (641.5 eV) and Mn 2p3/2 (653.8 eV) peaks (Song et al., 2014). The relatively weak peaks manifest that the content of manganese in the overall material is low, conforming to the

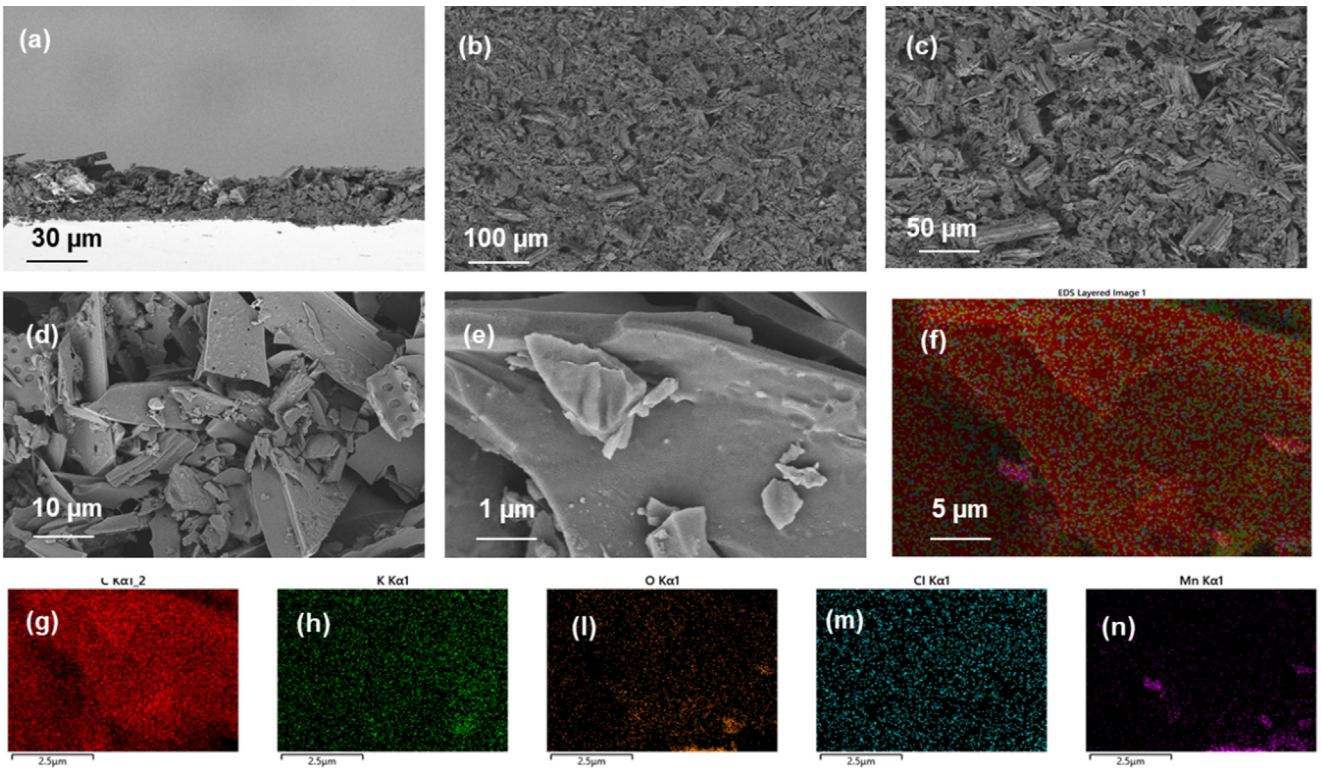

Fig. 4 a-e) sem images of bcm separators at different scales, and f-n) eds-mapping images of different elements.

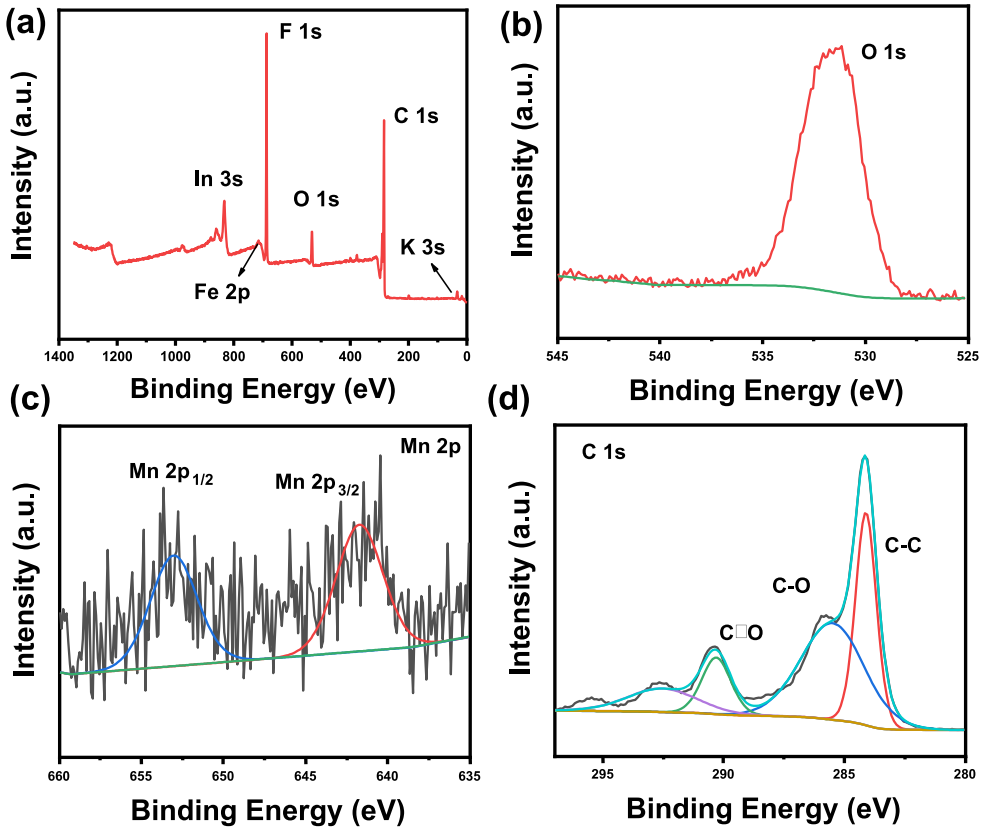

Fig. 5 a) Full XPS spectra, b) O 1 s, c) Mn 2p, d) C 1 s for BCM.

XRD results of C. The carbon peaks can be divided into C–C, C-O, and C = O peaks, which indicates that biomass materials are rich in organic functional groups (Chen et al., 2019). The adsorption of these functional groups of lithium polysulfides provides adsorption sites, which in turn promotes the transformation of lithium polysulfides and enhances the kinetic transformation of lithium-sulfur batteries. In addition, the K element is characterized with strong characteristic peaks at 295.8 eV, 292.8 eV and 291.1 eV, which are caused by the potassium element in the biomass (Figure S9). Moreover, the result is in line with the SEM result (Yang et al., 2018).

The contact angle test was conducted to test the affinity of the electrolyte with the separator. As shown in Figure S10, the contact angle (11 degrees) of our prepared separator with the electrolyte is smaller than that of the PP with the electrolyte (17.5 degrees), providing that the provided separator has excellent wettability and can effectively disperse and dissolve the electrolyte solution, thereby facilitating the improvement of the kinetic rate of lithium-sulfur batteries.

To conform the ability of the separator to adsorb and promote the decomposition of lithium polysulfides, a visualization experiment of the decomposition of lithium polysulfides was performed. The prepared separator was placed in Li_2S_6 solution of the same concentration, and the color change was compared. After 24 h, the Li_2S_6 solution of the PP separator remained unchanged, while the color of the BCM separator faded seriously (Figure S11a), indicating that the lithium polysulfide has been adsorbed. The UV test of LiPSs after adsorption (Figure S11b) revealed that as expected, the peak intensity of LiPSs was much lower than that of LiPSs and PP separators, implying that lithium polysulfides are adsorbed and catalyzed, which is favorable for improving the reaction kinetics of the battery (Ismail et al., 2001).

Therefore, CV testing was performed to validate the battery kinetics results. The CV curves of the symmetric cells are shown in Fig. 6a. In the cells without Li_2S_8, there is no redox peak, suggesting that no electrochemical reaction occurs. After adding Li_2S_8 solution, it can be seen that the redox peak area of the BCM is much larger than that of conventional conductive carbon (super p), indicating that the BCM provides high catalytic activity for the reaction of lithium polysulfide and effectively improves the redox of sulfur, conforming to the experimental results of polysulfide lithium adsorption visualization experiments (Luo et al., 2017).

At the same time, different separator cells were tested by cyclic voltammetry, as shown in Fig. 6b. The BCM redox peaks overlap very well, while the LiS scan peak intensities vary (Fig. 6c), which reveals that the BCM adsorbs lithium polysulfides and provides high catalytic activity for the reaction of lithium polysulfides, effectively enhancing the sulfur redox kinetics, and resulting in excellent battery stability. A similar situation appears in the CV curves at high scan rates (Figure S12).

In addition, the diffusion rate of Li^+ was also systematically investigated by measuring the CV curves of different separator cells at different scan rates from 0.1 to 0.3 mV s (Fig. 6d, e). Fig. 6g-i display the linear relationship between the peak current and the square root of the scan rate. According to the Randles-Sevcik equation $Ip = (2.69 \times 105) \cdot n^{1.5} \cdot S \cdot D_{Li+} 0.5 \cdot C_{Li} \cdot v^{0.5}$, the diffusion coefficient is proportional to the square of the peak current (Luo et al., 2017). In this equation, Ip refers to the peak current (A); n represents the number of electrons transferred in the reaction; S signifies the area of the electrode material; D_{Li+} provides the diffusion coefficient of L^{i+}; C_{Li} represents the concentration of Li^+ in the cathode, and ν means the scan rate. From the slope of the fitted line, the lithium-ion diffusion coefficient can be observed. Moreover, the BCM is faster than LiS, demonstrating that the BCM can effectively enhance the redox kinetics of sulfur (Cui et al., 2020).

Fig. 6f displays the EIS spectra of different batteries. The figure shows that they all show a typical Nyquist diagram, which is composed of a semi-circle in the high-frequency region and a diagonal line in the low-frequency region. In the low frequency region, BCM cells exhibit lower Warburg impedance. Since the Warburg impedance in the full cell is controlled by the diffusion of ions in the cathode, it is suggested that the BCM has a lower lithium-ion diffusion coefficient, conforming to the CV results. In the high frequency region, the charge transfer impedance Rct of the BCM is smaller, which suggests that the impedance of the interfacial layer is dramatically reduced due to the excellent ionic conductivity of the BCM (Xie et al., 2021).

The electrochemical rate performance is shown in Fig. 7a, and the modified sample has excellent electrochemical rate performance. The discharge capacity reached 1495.37 mAh g^{-1} in the first cycle at 0.1C. With the increasing charge and discharge rate, the discharge capacities were 1215.355 mAh g^{-1} (0.2C), 1136.367 mAh g^{-1} (0.5C), 1024.429 mAh g^{-1} (1C), 942.926 mAh g^{-1}(1.5C), 877.795 mAh g^{-1}(2.0C), 825.6977 mAh g^{-1}(2.5C), 769.653 mAh g^{-1}(3.0C), 688.774 mAh g^{-1}(3.5C), and 536.658 mAh g^{-1} (4.0C), reaching 1215.355 mAh g^{-1} (0.2C) after cycling. Compared with the original samples, the rate performance is improved significantly, and the carbon materials are rich in organic functional groups. The abundant functional groups can provide adsorption sites for the adsorption of lithium polysulfides. Meanwhile, the single crystal MnO with the exposed (1 1 1) crystal plane dispersed on the biomass carbon is characterized with high catalytic activity and chemical adsorption capacity, which tremendously enhances the kinetics of the battery. Due to the two interactions between the spin-up filled orbitals and the MnO filled orbitals, the directional decomposition of lithium polysulfides is stimulated, and the rate performance of lithium-sulfur batteries is improved. To further investigate the high rate cycling performance of the battery, the cycling performance of materials was tested at 2C and 4C. As shown in Fig. 7b, due to the excellent electrical conductivity, the battery has a very high capacity close to 800 mAh g^{-1} in the initial cycle of 2C, and still possesses a high capacity (500 mAh g^{-1}) after 500 times of charge and discharge with the high discharge efficiency (80%) and low single-turn decay rate (0.05%). Moreover, our material has a capacity of 600mAh g^{-1} at a high current at 4C and can be cycled stably for 500 times at 4C. After 500-cycles, the cycle still has a capacity of 300 mAh g^{-1}, which also demonstrates that the BCM dramatically improves the kinetics of the lithium-sulfur battery that exhibits obvious advantages compared with the data reported in the literature. Furthermore, high dynamics is a necessary condition under marketization (Yang et al., 2012). However, as shown in Fig. 7b, we can see that the electrochemical performance is not particularly smooth, especially in the 4C condition. This reason may be that under high current, due to the insulating properties of sulfur, the electrochemical reaction is difficult to occur rapidly in

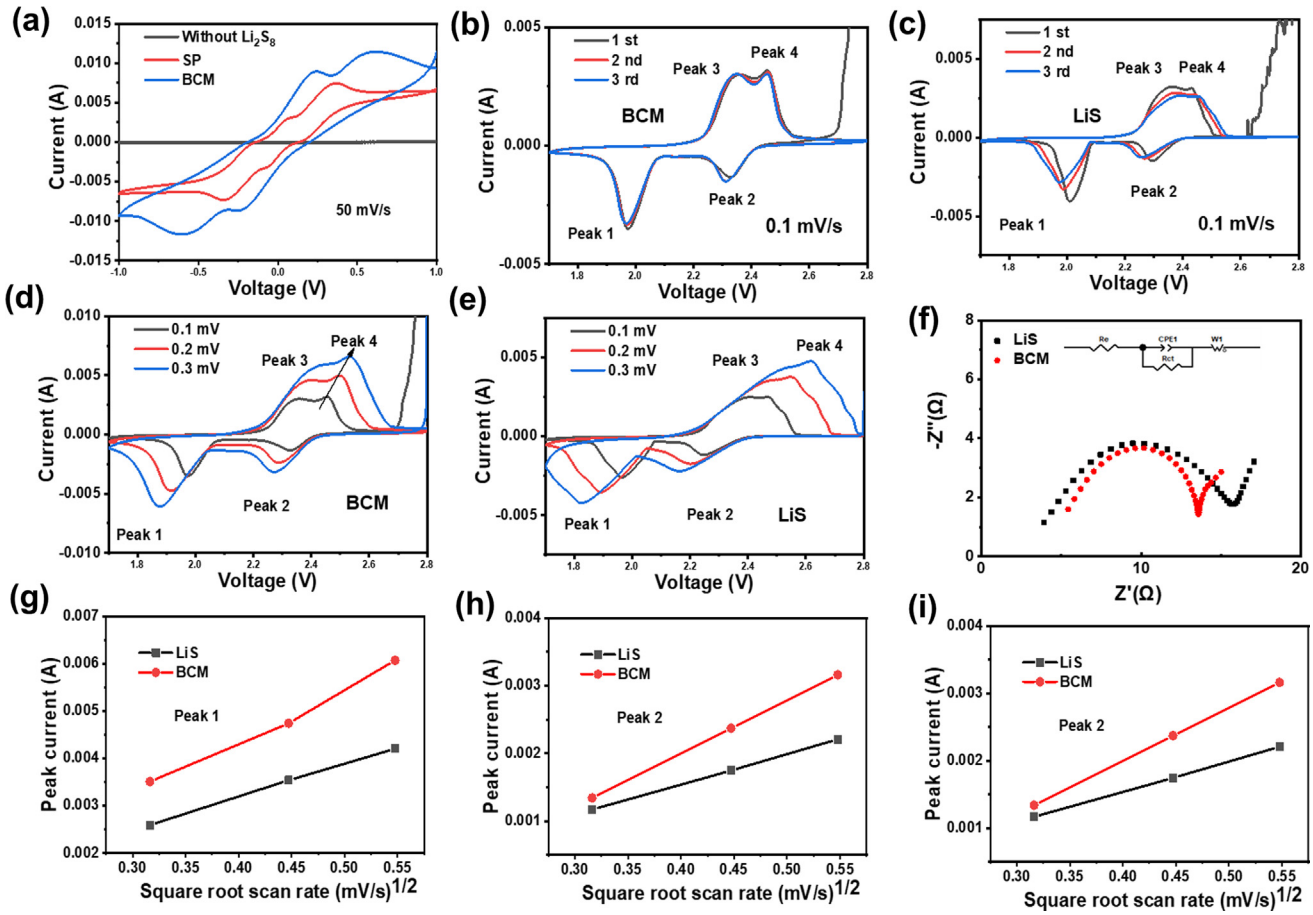

Fig. 6 CV profiles of a) symmetric cell, b) BCM and c) LiS at the scanning rates of 0.1 mV, d) BCM and e) LiS at various scanning rates, f) EIS contrast curves, g-i) reaction kinetics with respect to the Li^+ ion diffusion properties of the BCM and LiS at various scan rates.

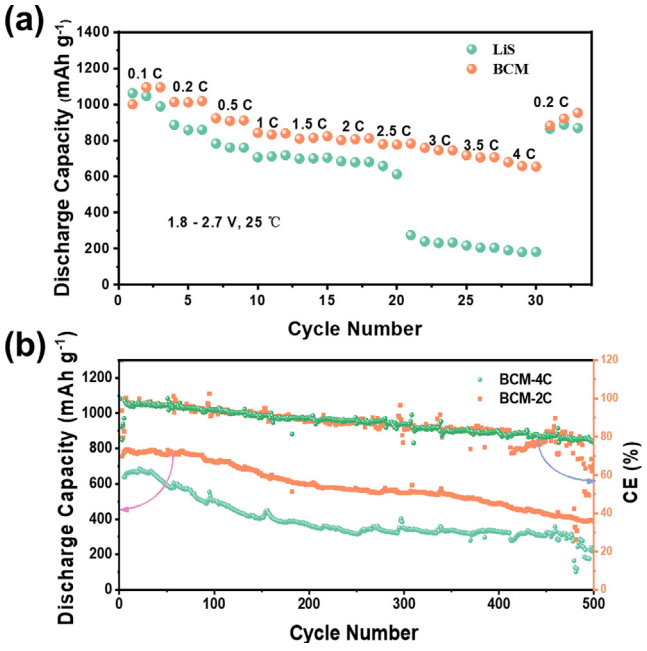

Fig. 7 a) rate capacities of bcm and LiS, b) cycling performances of BYM in the voltage range of 1.7–2.8 V at 2C and 4C.

a short period of time, resulting in fluctuations in coulombic efficiency, which in turn cause changes in discharge capacity.

The discharge curves of different cycles at different rates are shown in Figure S13. Based on the figure, it can be seen that at 2C, the battery can maintain a relatively stable voltage platform, and at 4C, the voltage platform has a slight decrease, displaying that the modified separator exhibits excellent stability under large magnification. Furthermore, under the 2C condition, the huge voltage plateau drop of the pristine lithium-sulfur battery occurs, which demonstrates that the material is featured with the higher polarization, which decreases the stability of the battery.

The mechanism is presented in Fig. 8. In conventional lithium-sulfur batteries, due to the low conductivity of sulfur and its lithium compounds, the solid–liquid reaction stage (S_8-$Li_2S_{4\text{-}8}$) and the liquid–solid reaction stage (Li_2S_4-$_8$-Li_2S) are facing a huge energy barrier that hinders the improvement concerning the rate performance of lithium-sulfur batteries and also influences the practical application of lithium-sulfur batteries. Here, a carbon separator with MnO supported on biomass carbon was fabricated, when MnO was the single crystal, and the exposed surface was the (1 1 1) crystal plane with the highest catalytic and adsorption activity. Furthermore, due to the two interactions between the spin-up filled orbitals and the MnO filled orbitals, the directional decompo-

Fig. 8 The functional mechanism of BCM separator.

sition of lithium polysulfides is promoted and the rate performance of lithium-sulfur batteries is improved.

3. Experimental

Biomass carbon was converted by *Phragmites australis*: The reed stems were dried and kept warm with Mn_2O_3 (mass ratio 95:5) for two hours in argon at 800 degrees Celsius.

The preparation of the microporous carbon separator. The biomass carbon obtained above was mixed with PVDF at mass ratio 90:10 dissolved with NMP (N-Methyl Pyrrolidone) to produce a thick paste, coated on the diaphragm with a thickness of 20 μm (Celgard 2400), followed by being vacuum-dried at 80 degrees Celsius. Next, it was named as the BCM (Biomass Carbon MnO separator).

Preparation of Cathode: Sulfur (80 wt%) and super p (20 wt%) were calcined at 155 degreesC for 12 h under argon. The material, acetylene black, and PVDF were mixed at a ratio of 8:1:1, and coated on aluminum foil to obtain cathode.

Assembly of button batteries: The button battery is assembled in a glove box filled with argon, and the electrolyte is 1 M LiTFSI in DME: DOL (1:1 vol%) with 1 M $LiNO_3$.

Electrochemical test: The voltage range of cycle performance and ratio performance is 1.7–2.8 V. In addition, CV test scanning speed is 0.1 mV, while the voltage range is 1.7–2.8 V. Furthermore, EIS impedance test frequency varies from 100 mHz to 100 kHZ.

3.1. Characterization analysis

Structural analysis was conducted by X-ray diffraction (XRD) measurements. The surface structure was analyzed by the scanning electron microscope (SEM), whereas surface elemental analysis was performed by X-ray photoelectron spectroscopy (XPS).

3.2. The theoretical calculation

The experimental details are included in the *Supporting Information*.

4. Conclusion

To conclude, in this study, the DFT calculation is performed to predict the formation of MnO on the biochar made from *Phragmites australis*. The adsorption energy and catalytic capacity of MnO with different crystal planes for lithium polysulfide are also measured. The results demonstrate that the MnO (1 1 1) crystal plane has the highest chemical adsorption energy and catalytic energy. In addition, the anchoring and catalytic method to lithium polysulfides, such as the interaction between the filled orbital of lithium polysulfide with the spin-up and that of MnO (1 1 1), and the transfer of electrons from Li_2S_6 to the empty orbital (spin-down) of Mn between the frontier orbitals are further investigated. Moreover, a MnO-loaded biomass carbon separator is prepared, and experiments including electrochemical tests and CV tests proved that the prepared biomass carbon separator enhances the kinetic reaction to a large degree.

Declaration of Competing Interest

The authors declare that they have no known competing financial interests or personal relationships that could have appeared to influence the work reported in this paper.

Acknowledgments

This study was supported by Hubei University of Science and Technology Research and Development Fund (BK202001), Hubei Provincial Natural Science Foundation of China (2021CFB112), Special scientific research project of Hubei Provincial Key Laboratory of Radiation Chemistry and Functional Materials (2022ZX09) and Innovation team of Hubei University of Science and Technology (2022T02).

Appendix A. Supplementary material

Supplementary data to this article can be found online at https://doi.org/10.1016/j.arabjc.2023.104752.

References

Cao, K., Liu, H., Li, Y., Wang, Y., Jiao, L., 2017. Encapsulating sulfur in δ-MnO2 at room temperature for Li-S battery cathode. Energy

Storage Mater. 9, 78–84. https://doi.org/10.1016/j.ensm.2017.06.012.

Chang, J., Shang, J., Sun, Y., Ono, L.K., Wang, D., Ma, Z., Huang, Q., Chen, D., Liu, G., Cui, Y., Qi, Y., Zheng, Z., 2018. Flexible and stable high-energy lithium-sulfur full batteries with only 100% oversized lithium. Nat. Commun. 9, 4480. https://doi.org/10.1038/s41467-018-06879-7.

Chen, H., Pei, A., Lin, D., Xie, J., Yang, A., Xu, J., Lin, K., Wang, J., Wang, H., Shi, F., Boyle, D., Cui, Y., 2019. Uniform high ionic conducting lithium sulfide protection layer for stable lithium metal anode. Adv. Energy Mater. 9. https://doi.org/10.1002/aenm.201900858.

Cui, Y., Liu, S., Wang, D., Wang, X., Xia, X., Gu, C., Tu, J., 2020. A facile way to construct stable and ionic conductive lithium sulfide nanoparticles composed solid electrolyte interphase on Li Metal Anode. Adv. Funct. Mater. https://doi.org/10.1002/adfm.202006380.

Guo, W., Han, Q., Jiao, J., Wu, W., Zhu, X., Chen, Z., Zhao, Y., 2020. In situ construction of robust biphasic surface layers on lithium metal for lithium-sulfide batteries with long cycle life. Angew. Chem. Int. Ed. Engl. https://doi.org/10.1002/anie.202015049.

He, C., Liang, Y., Zhang, W., 2022. Design of novel transition-metal-doped C6N2 with high-efficiency polysulfide anchoring and catalytic performances toward application in lithium-sulfur batteries. ACS Appl. Mater. Interfaces 14, 29120–29130. https://doi.org/10.1021/acsami.2c07285.

He, C., Qi, Z.F., Zhang, W.X., 2023. Design of transition metal carbonitrides (MCNs) as promising anchoring and high catalytic performance materials for lithium-sulfur batteries. J. Alloys Compd. 934. https://doi.org/10.1016/j.jallcom.2022.167786.

Ismail, I., Noda, A., Nishimoto, A., Watanabe, M., 2001. XPS study of lithium surface after contact with lithium-salt doped polymer electrolytes. Electrochim. Acta 46, 1595–1603. https://doi.org/10.1016/S0013-4686(00)00758-1.

Li, T., He, C., Zhang, W., 2020. Two-dimensional porous transition metal organic framework materials with strongly anchoring ability as lithium-sulfur cathode. Energy Storage Mater. 25, 866–875. https://doi.org/10.1016/j.ensm.2019.09.003.

Li, T., He, C., Zhang, W., 2021. Rational design of porous carbon allotropes as anchoring materials for lithium sulfur batteries. J. Energy Chem. 52, 121–129. https://doi.org/10.1016/j.jechem.2020.04.042.

Li, H., Ma, S., Cai, H., Zhou, H., Huang, Z., Hou, Z., Wu, J., Yang, W., Yi, H., Fu, C., Kuang, Y., 2019. Ultra-thin Fe3C nanosheets promote the adsorption and conversion of polysulfides in lithium-sulfur batteries. Energy Storage Mater. 18, 338–348. https://doi.org/10.1016/j.ensm.2018.08.016.

Liang, X., Hart, C., Pang, Q., Garsuch, A., Weiss, T., Nazar, L.F., 2015. A highly efficient polysulfide mediator for lithium-sulfur batteries. Nat. Commun. 6, 5682. https://doi.org/10.1038/ncomms6682.

Louli, A.J., Coon, M., Genovese, M., deGooyer, J., Eldesoky, A., Dahn, J.R., 2021. Optimizing cycling conditions for anode-free lithium metal cells. J. Electrochem. Soc. 168,. https://doi.org/10.1149/1945-7111/abe089 020515.

J. Luo, R.-C. Lee, J.-T. Jin, Y.-T. Weng, C.-C. Fang, N.-L. Wu, A dual-functional polymer coating on a lithium anode for suppressing dendrite growth and polysulfide shuttling in Li-S batteries, Chem. Commun. (Cambridge, U. K.) 53 (2017), 963-966, 10.1039/c6cc09248a

D. Luo, C.J. Li, Y.G. Zhang, Q.Y. Ma, C.Y. Ma, Y.H. Nie, M. Li, X. F. Weng, R. Huang, Y. Zhao, L.L. Shui, X. Wang, Z.W. Chen, Design of Quasi-MOF Nanospheres as a Dynamic Electrocatalyst toward Accelerated Sulfur Reduction Reaction for High-Performance Lithium-Sulfur Batteries, Adv. Mater. 34 (2022), ARTN 210554110.1002/adma.202105541

P. Manasa, Z.J. Lei, F. Ran, Biomass Waste Derived Low Cost Activated Carbon from Carchorus Olitorius (Jute Fiber) as Sustainable and Novel Electrode Material, J Energy Storage 30 (2020), ARTN 101494 10.1016/j.est.2020.101494.

Mohan, E.H., Sarada, B.V., Naidu, R.V.R., Salian, G., Haridas, A.K., Rao, B.V.A., Rao, T.N., 2016. Graphene-modified electrodeposited dendritic porous tin structures as binder free anode for high performance lithium-sulfur batteries. Electrochim. Acta 219, 701–710. https://doi.org/10.1016/j.electacta.2016.10.042.

Nair, R.R., Mondal, M.M., Weichgrebe, D., 2020. Biochar from co-pyrolysis of urban organic wastes-investigation of carbon sink potential using ATR-FTIR and TGA. Biomass Convers. Biorefinery. https://doi.org/10.1007/s13399-020-01000-9.

Z.H. Shen, M.Q. Cao, Z.L. Zhang, J. Pu, C.L. Zhong, J.C. Li, H.X. Ma, F.J. Li, J. Zhu, F. Pan, H.G. Zhang, Efficient Ni2Co4P3 Nanowires Catalysts Enhance Ultrahigh-Loading Lithium-Sulfur Conversion in a Microreactor-Like Battery, Adv. Funct. Mater. 30 (2020), ARTN 190666110.1002/adfm.201906661

X.Y. Shi, L.W. Yang, S. Li, Y. Wang, X.Y. Chen, Z.G. Wu, Y.J. Zhong, Y.X. Chen, S.Y. Gao, G.K. Wang, X.D. Guo, B.H. Zhong, Promoting electrochemical kinetics of Li-S batteries with C@SnS2 modified separator via synergic effect between porous carbon matrix and polar SnS2, Electrochim. Acta 390 (2021), ARTN 13882910.1016/j.electacta.2021.138829.

Song, T.T., Cai, W.M., Jin, Q.L., Feng, W.L., Fan, L.J., Shen, Y.Y., Fang, H., Tian, F.F., 2014. Comparison of microbial communities and histological changes in Phase I rice straw-based Agaricus bisporus compost prepared using two composting methods. Scient. Horticult. 174, 96–104. https://doi.org/10.1016/j.scienta.2014.05.012.

Wang, L., Mao, J.G., Zhao, H.J., Li, M., Wei, Q.S., Zhou, Y., Shao, H.P., 2016. Comparison of characterization and microbial communities in rice straw- and wheat straw-based compost for Agaricus bisporus production. J. Ind. Microbiol. Biotechnol. 43, 1249–1260. https://doi.org/10.1007/s10295-016-1799-6.

Wei, Z., Yifan, L., Haifeng, L., Shuai, X., Jiawen, Z., Junjie, X., Hongchang, J., Xianghua, K., Song, J., Haiyan, W., Xiaojun, W., Hengxing, J., 2023. A comparison study of the electrocatalytic sulfur reduction activity on heteroatom-doped graphene for Li–S battery. Small Struct. https://doi.org/10.1002/sstr.202200244.

Wu, Y., He, C., Zhang, W., 2021. Novel design strategy of high activity electrocatalysts toward nitrogen reduction reaction via boron–transition-metal hybrid double-atom catalysts. ACS Appl. Mater. Interfaces 13, 47520–47529. https://doi.org/10.1021/acsami.1c11889.

Wu, Y., He, C., Zhang, W., 2022. "Capture-backdonation-recapture" mechanism for promoting N2 reduction by heteronuclear metal-free double-atom catalysts. J. Am. Chem. Soc. 144, 9344–9353. https://doi.org/10.1021/jacs.2c01245.

Xiaohui, T., Yunnian, C., Yingke, Z., Bingyin, Z., Guiru, W., 2023. Long-cycling and high-loading lithium-sulfur battery enabled by free-standing three-dimensional porous NiCo2O4 nanosheets. Appl. Energy. https://doi.org/10.1016/j.apenergy.2023.120694.

Xiaowan, P., Baigang, A., Shumin, Z., Bao, W., 2023. Synergistic enhancement of Li-S battery low-temperature cycling performance by nano-sized uniformly compounded FeCoNi and MnO nanoparticles. Chem. Eng. J. https://doi.org/10.1016/j.cej.2023.141445.

Xie, Y., Cao, J., Wang, X., Li, W., Deng, L., Ma, S., Zhang, H., Guan, C., Huang, W., 2021. MOF-derived bifunctional Co0.85Se nanoparticles embedded in N-doped carbon nanosheet arrays as efficient sulfur hosts for lithium-sulfur batteries. Nano Lett. 21, 8579–8586. https://doi.org/10.1021/acs.nanolett.1c02037.

Yang, Y., Zheng, G., Misra, S., Nelson, J., Toney, M.F., Cui, Y., 2012. High-capacity micrometer-sized Li2S particles as cathode materials for advanced rechargeable lithium-ion batteries. J. Am. Chem. Soc. 134, 15387–15394. https://doi.org/10.1021/ja3052206.

Yang, Y., Sun, K., Han, L.F., Jin, J., Sun, H.R., Yang, Y., Xing, B.S., 2018. Effect of minerals on the stability of biochar. Chemosphere 204, 310–317. https://doi.org/10.1016/j.chemosphere.2018.04.057.

Yucheng, F., Rajesh, K.S., Shuo, F., Jun, L., Jie, X., Jie, B., Zhijie, X., Dongping, L., 2023. Understanding of low-porosity sulfur electrode for high-energy lithium-sulfur batteries. Adv. Energy Mater. https://doi.org/10.1002/aenm.202203386.

Zhang, R., Chen, X., Shen, X., Zhang, X.-Q., Chen, X.-R., Cheng, X.-B., Yan, C., Zhao, C.-Z., Zhang, Q., 2018. Coralloid carbon fiber-based composite lithium anode for robust lithium metal batteries. Joule 2, 764–777. https://doi.org/10.1016/j.joule.2018.02.001.

Zhang, L., Liu, D., Muhammad, Z., Wan, F., Xie, W., Wang, Y., Song, L., Niu, Z., Chen, J., 2019. Single nickel atoms on nitrogen-doped graphene enabling enhanced kinetics of lithium-sulfur batteries. Adv. Mater. 31. https://doi.org/10.1002/adma.201903955.

Zhang, P., Zhao, Y., Li, Y., Li, N., Silva, S.R.P., Shao, G., Zhang, P., 2023. Revealing the selective bifunctional electrocatalytic sites via in situ irradiated X-ray photoelectron spectroscopy for lithium-sulfur battery. Adv. Sci. https://doi.org/10.1002/advs.202206786.

Zhao, Q., Tu, Z., Wei, S., Zhang, K., Choudhury, S., Liu, X., Archer, L.A., 2018. Building organic/inorganic hybrid interphases for fast interfacial transport in rechargeable metal batteries. Angew. Chem.-Int. Ed. 57, 992–996. https://doi.org/10.1002/anie.201711598.

Zheng, J., Fan, X., Ji, G., Wang, H., Hou, S., DeMella, K.C., Raghavan, S.R., Wang, J., Xu, K., Wang, C., 2018. Manipulating electrolyte and solid electrolyte interphase to enable safe and efficient Li-S batteries. Nano Energy 50, 431–440. https://doi.org/10.1016/j.nanoen.2018.05.065.

Zu, C., Dolocan, A., Xiao, P., Stauffer, S., Henkelman, G., Manthiram, A., 2016. Breaking down the crystallinity: the path for advanced lithium batteries. Adv. Energy Mater. 6. https://doi.org/10.1002/aenm.201501933.